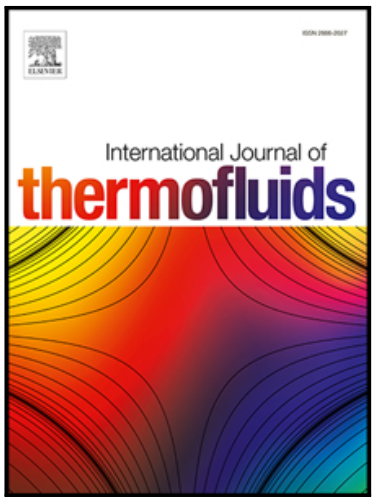

MHD Analysis of Couple Stress Nanofluid through a Tapered Non-Uniform Channel with Porous Media and Slip-Convective Boundary Effects

P. Deepalakshmi , G. Shankar , E.P. Siva , D. Tripathi , O. Anwar Bég Professor and Director

PII: S2666-2027(25)00155-7
DOI: https://doi.org/10.1016/j.ijft.2025.101208
Reference: IJTF 101208

To appear in: *International Journal of Thermofluids*

Received date: 30 November 2024
Revised date: 12 March 2025
Accepted date: 7 April 2025

Please cite this article as: P. Deepalakshmi , G. Shankar , E.P. Siva , D. Tripathi , O. Anwar Bég Professor and Director , MHD Analysis of Couple Stress Nanofluid through a Tapered Non-Uniform Channel with Porous Media and Slip-Convective Boundary Effects, *International Journal of Thermofluids* (2025), doi: https://doi.org/10.1016/j.ijft.2025.101208

MHD Analysis of Couple Stress Nanofluid through a Tapered Non-Uniform Channel with Porous Media and Slip-Convective Boundary Effects

P. Deepalakshmi[1], G. Shankar[2], E. P. Siva[3,*], D. Tripathi[4] and O. Anwar Bég[5]

[1,2,3] Department of Mathematics, College of Engineering and Technology, SRM Institute of Science and Technology, Kattankulathur – 603203, Tamil Nadu, India. dp5497@ srmist.edu.in, sg1710@ srmist.edu.in, sivae@srmist.edu.in.*

[4]Department of Mathematics, National Institute of Technology, Uttarakhand-246174, India. dtripathi@nituk.ac.in

[5]Professor and Director - Multi-Physical Engineering Sciences Group, Dept. Mechanical and Aeronautical Engineering, Corrosion/Coatings Lab, 3-08, SEE Building, Salford University, Manchester, M54WT, UK. O.A.Beg@salford.ac.uk

[*]Corresponding Author E. Mail Id: sivae@srmist.edu.in

Abstract: The current research addresses the peristaltic transport mechanism that propels fluid through a conduit through rhythmic contraction and relaxation of the conduit walls, a phenomenon evident in numerous biological systems, including the gastrointestinal tract. Motivated by applications in nano-pharmacological drug delivery and thermo-biomagnetic therapy, a mathematical and computational analysis of radiative heat transfer in peristaltic pumping of a magnetohydrodynamic (MHD) couple stress nanofluid through a tapered asymmetric passage, with the influences of a porous medium and wall slip, is presented. Buongiorno's two-component nanoscale model is deployed and the Stokes couple stress non-Newtonian model utilized. Physically the porous medium is modelled with a drag force formulation and simulates the presence of obstructions and deposits in the gastric tract and blood vessels. The governing equations for the couple stress nanofluid are reduced by employing the long-wavelength approximation and the low Reynolds number condition, both standard approaches in fluid dynamics research. Analytical solutions are derived for axial velocity, temperature profile, nanoparticle concentration, stream function, and pressure gradient, providing a comprehensive understanding of the flow dynamics. Furthermore, numerical integration methods are utilized to calculate the average pressure increase (ΔP) and the heat transfer coefficient (Z). The impact of critical parameters namely the Hartmann number (M), Brownian motion parameter (N_b),

thermophoresis parameter (N_t), Prandtl number (Pr), slip parameter (L) and radiation parameter (R_n) on fluid dynamics is examined through comprehensive graphical representations. The findings indicate that peristaltic pumping efficiency is superior in a uniform channel relative to a non-uniform channel, underscoring the influence of channel geometry on flow performance. Moreover, the synergistic effects of thermophoresis and Brownian motion result in a substantial elevation of fluid temperature, enhancing thermal energy transfer throughout the system. Increasing wall slip parameter diminishes the friction between the fluid and the channel walls, facilitating smoother fluid flow and decreasing thermal resistance. Stronger radiative heat flux promotes energy absorption in the system, resulting in accelerated fluid cooling at the boundary of the conduit (channel). Increasing non-uniformity parameter associated with asymmetry (m) leads to a diminished nanoparticle concentration. Increasing Brownian motion nanoscale parameter elevates nanoparticle concentrations. A strong modification is also computed with thermophoretic nanoscale parameter. Heat transfer coefficient displays oscillatory behavior attributable to the contraction and expansion of the channel walls. The complete flow zone is categorized into four quadrants (peristaltic pumping zone, increased flow zone, free pumping zone and retrograde pumping zone) based on the pressure difference (ΔP) and time average of the flux over one period of the wave (Θ), each indicating a distinct flow behavior. Increasing Hartmann magnetic number augments peristaltic pumping. An increase in Grashof number (Gr) i.e. thermal buoyancy parameter correlates with enhanced pumping throughout all four quadrants. This study offers significant insights into enhancing peristaltic transport processes in industrial, medicinal, and environmental contexts, especially concerning MHD nanofluids inside intricate geometries featuring porous media and slip circumstances.

Key words: Brownian motion and Thermophoresis parameter; Peristalsis; Tapered nonuniform channel; Thermal radiation; Couple stress fluid.

1. Introduction

Recently, researchers have exhibited an increased interest in the study of the peristaltic movement, motivated by its expanding uses in industry and medicine. Peristalsis, a mechanism of fluid transport, is essential for numerous bodily functions, including the movement of urine from the kidneys to the bladder, the transportation of food through the esophagus, the regulation of blood flow in small vessels, and the facilitation of bile, lymphatic fluid, and chyme movement in the

digestive system. This natural mechanism is essential to the functioning of medical devices such as dialysis machines, blood pumps, and heart-lung systems. Peristaltic flow has consistently captivated researchers because of its essential function in numerous biological and commercial processes. Latham [1] basic experimental research established the basis for extensive studies on peristaltic transport across diverse flow conditions and geometries. Shapiro and Jaffrin [2] established a significant early mathematical model that analyzed peristaltic flow based on long wavelength and low Reynolds number assumptions. This foundational work facilitated future investigation into more intricate flow conditions. Radhakrishnamacharya and Radhakrishnamurty [3] did a heat transfer analysis in peristaltic transport across non-uniform channels, whereas Gupta and Sheshadri [4] examined the challenges of peristaltic pumping in non-uniform tubes. Eytan and Elad [5] offered significant insights into fluid dynamics by examining intra-uterine fluid movements induced by uterine contractions in a non-pregnant uterus. Further research, including that of Srinivas and Kothandapani [6], investigated the heat transfer phenomena in peristaltic transport within asymmetric channels, while Muthuraj and Srinivas [7] examined magnetohydrodynamic oscillatory flow with heat transfer in undulating channels. Peristaltic transport in non-Newtonian fluids has gained significant attention due to its importance in biological systems, beyond the study of Newtonian fluids. The couple-stress fluid theory, initially introduced by Stokes [8], offers a framework for comprehending the intricate rheological behavior of these fluids. This theory has been applied to biological situations, such as blood flow, with Chaturani [9] examining the viscosity of Poiseuille flow for couple-stress fluids, and Srivastava [10] analyzing the peristaltic transport of these fluids. Mekheimer [11] further investigated couple-stress fluid transport in both uniform and non-uniform channels, enhancing the comprehension of these flows in medical applications. Sobh [12] recently examined the impact of coupling tensions and slip flow on peristaltic transport in both uniform and non-uniform channels, contributing to the expanding body of knowledge.

Nanofluids, pioneered by Choi [13], signify a new frontier in fluid dynamics research. These fluids, composed of nanoparticles dispersed in a base liquid, have improved thermal conductivity and distinctive flow properties, rendering them appropriate for numerous industrial and biological applications. Choi et al. [14] established that micrometer-sized particles were ineffective for heat transfer in real applications, while nanoparticles markedly enhance thermal conductivity without

obstructing flow pathways. Buongiorno [15] highlighted the critical role of Brownian diffusion and thermophoresis in the mechanics of slip flow involving nanofluids. Nanofluids, particularly those containing metallic nanoparticles such as silver, copper, and aluminum, demonstrate potential use in confined spaces where efficient heat transfer is essential. Nadeem and Akram [16] conducted a further investigation into heat transfer in peristaltic flows of magnetohydrodynamic fluids with partial slip, enhancing the comprehension of nanofluid transport in restricted settings. The biological applications of nanofluids are substantial. Magnetic cell separation, medication delivery, and contrast enhancement in magnetic resonance imaging are several applications. Prakash et al. [17] and Landeghem et al. [18] investigated the application of magnetic nanoparticles in medical diagnostics, thermotherapy, and imaging, whereas Tripathi and Anwar [19] examined the function of nanofluids in drug delivery systems. Akbar and Nadeem [20, 21] explored the peristaltic flow of nanofluids in arteries and intestines, including slip effects and the stress-strain characteristics of the fluid. Their updated research [22] examined the flow of nanofluids in non-uniform tubes, emphasizing the influence of slip and temperature effects on peristaltic transport.

Subsequent inquiries into MHD peristaltic flow have revealed the impact of nanoparticle interactions with biological systems. Nadeem et al. [23] examined the effects of temperature and also with velocity slip on magnetohydrodynamic peristaltic flow, incorporating carbon nanotubes within asymmetric channels. Nadeem and Ijaz [24] inspected the influence of metallic nanoparticles on blood circulation in arteries impacted by stenosis and aneurysm, illustrating the potential of nanofluids in biomedical applications. Aly and Ebaid [25] surveyed the influence of velocity second slip boundary conditions on the peristaltic flow of nanofluids in asymmetric channels, enhancing the comprehension of flow dynamics in practical applications. Furthermore, Habibi et al. [26] emphasised the influence of a high-gradient magnetic field on nanoparticle distribution within pulsatile blood flow, demonstrating the prospective applications of nanotechnology in medical therapies. Deepalakshmi et al. [27, 28] offered significant insights into the intricate dynamics of electromagnetic peristaltic flow along with wall properties involving multi-phase non-Newtonian thermo-solutal transport. Their study highlighted the application of magnetic fields, combined with an understanding of the Hall effect, can effectively control the behaviour of non-Newtonian fluid flow. Precise solutions addressing the influence of Hall current and thermal radiation on oscillatory Darcy blood flow in a stenosed artery was characterized by

Shankar et al. [29]. Kothandapani et al. [30] investigated the peristaltic motion of magnetohydrodynamic Carreau fluid in tapered asymmetric channels. The research proposed by Shankar et al. [31,32] aims to investigate blood flow in a stenosed artery modeled as a Newtonian fluid, taking into account the effects of a magnetic field, chemical reactions, thermal radiation, radiative heat flux, and a porous medium. Kothandapani and Prakash [33] analyzed Williamson nanofluids subjected to magnetic fields and thermal radiation. Nevertheless, these investigations failed to account for the distinct characteristics of couple-stress nanofluids within porous media. Rafiq and Khan [34,35] assessed the thermal and mass transfer features of nanofluids using the Buongiorno model, which accurately represents the effects of Brownian motion and thermophoretic diffusion, highlighting their unique qualities. The research investigates the dynamics of a magneto-couple stress nanofluid affected by chemical reaction within a peristaltically driven, symmetric, nonuniform channel. Alhazmi et al. [36] performed a comprehensive examination of a mathematical model for pair stress magneto-nanofluids, solving the governing equations of motion through long wavelength and low Reynolds number approximations, in light of its significance to biological flow dynamics. The investigation by Nisar et al. [37] explains the effects of thermally convective boundary conditions and zero mass flux constraints on flexible channel walls, emphasizing their significance in fluid flow analysis. Yasmin and Bilal et al. [38-40] emphasized that an increase in the thermophoresis coefficient intensifies the temperature distribution, as a higher concentration of particles enhances thermophoretic activity. These findings hold significant potential for medical applications, particularly in nanoparticle-based drug delivery systems for targeting cancer cells. A clear understanding of the peristaltic mechanism is essential for analyzing various biological flow systems. Akram et al. [41,42] conducted a numerical investigation into the double-diffusive peristaltic flow of a non-Newtonian six-constant Jefferys nanofluid within an irregular medium. Additionally, Akram et al. [43-45] examined the distinctive rheological properties of magneto-pseudoplastic nanofluids, emphasising the impact of the pseudoplastic characteristics of nanoparticles and their interaction with a magnetic field on flow dynamics. Furthermore, they formulated a mathematical model for Sisko fluids and pseudoplastic nanofluids, integrating double-diffusive convection and an angled magnetic field with diverse waveforms, utilising a simple solution approach.

Despite previous studies which have examined different aspects of peristaltic pumping separately (e.g. nanofluids, magnetic body force, slip effects etc), the generalized multi-physical problem of magnetohydrodynamic (MHD) couple stress nanofluids within tapered asymmetric channels containing porous media (i.e. fatty deposits, obstructions etc) is still largely unexamined. This is the motivation for the present investigation, which fills the research gap by examining the peristaltic motion of MHD couple-stress nanofluids with wall slip in tapered asymmetric porous channels which is relevant to electromagnetic non-Newtonian flows in physiological systems. The current study also generalizes previous investigations by amalgamating multiple physics aspects including magnetohydrodynamics (MHD), non-Newtonian couple stress behaviour which can represent actual biofluids, porous medium drag effects, convective and radiative heat transfer, geometric asymmetry of blood vessels and wall slip effects, which provides a more comprehensive approach to actual medical fluid dynamics analysis. By applying the assumptions of long wavelength and low Reynolds number, the governing equations are streamlined, yielding analytical solutions for the flow variables. The impact of essential parameters on flow characteristics is subsequently examined, yielding new insights into this intriguing domain of biological fluid dynamics of relevance to pharmacology, thermo-magnetic therapy and other biomedical treatments. The necessity of well-defined research questions enhances the manuscript and also aim to the study's technical rigor and ensure its contribution to the field.

- How do magnetohydrodynamic (MHD) and couple stress effects influence the peristaltic transport of nanofluids in tapered asymmetric porous channels?
- What is the impact of slip boundary conditions on the flow dynamics and heat transfer characteristics of MHD couple stress nanofluids in physiological systems?
- How do porous medium drag effects (e.g., fatty deposits, obstructions) alter the peristaltic motion and thermal behavior of the nanofluid?
- In what manner do convective and radiative heat transfer mechanisms contribute to the overall energy distribution in the flow system?
- How do key non-dimensional parameters (e.g., Hartmann number, couple stress parameter, slip coefficient) affect velocity, temperature, and concentration profiles?

2. Mathematical Formulation

The peristaltic transport of a MHD couple stress nanofluid in an infinite two-dimensional tapered asymmetric porous channel with slip effects is studied herein. The effect of radiative heat transfer is also considered. The boundary of the left- and right-hand side walls are $Y = H_1(X,t')$ and $Y = H_2(X,t')$, where *(U)* and *(V)* are the velocities of axial and transverse directions respectively and *(X)* is the axial direction and *(Y)* is the transverse direction. The half width of the channel is d with the wave speed *(c)*. The channel walls are maintained at temperatures (T_0) and (T_1) respectively, which are high enough to induce radiative heat transfer. (C_0) and (C_1) denote the concentrations of the right and left side walls, respectively.

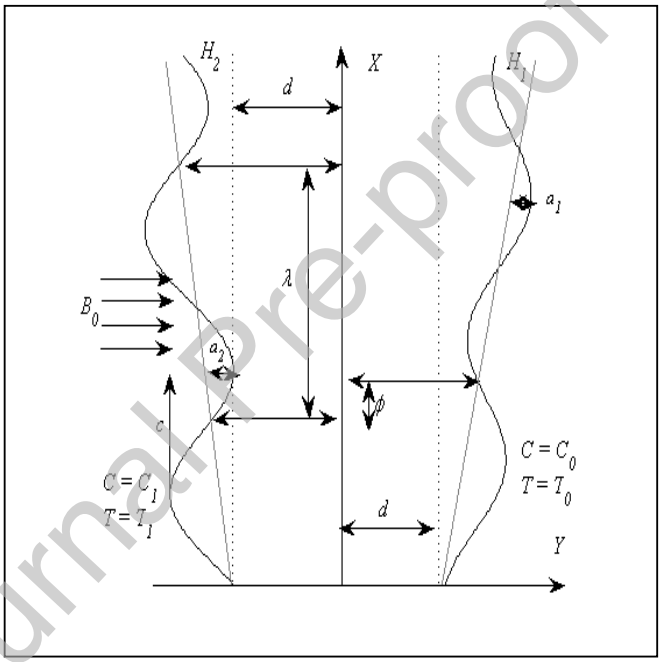

Fig. 1 Geometry of a tapered asymmetric channel

The channel boundaries are modelled by the following equations, which simulate sinsusoidal wave motions on the walls:

$$H_1(X,t') = d + m'X + a_1 \sin\left[\frac{2\pi}{\lambda}(X - ct')\right] \tag{1}$$

$$H_2(X,t') = -d - m'X - a_2 \sin\left[\frac{2\pi}{\lambda}(X - ct') + \phi\right] \tag{2}$$

Where (a_1) and (a_2) are the amplitudes of the right and left hand side walls, (λ) is the wavelength, the phase difference (ϕ) varies in the range $0 \le \phi \le \pi$, $\phi = 0$ that corresponds to the symmetric channel with waves out of phase and $\phi = \pi$ with waves in phase, and further (a_1), (a_2), *(d)* and (ϕ) satisfy the condition of the inlet of the divergent channel :

$$a_1^{\,2} + a_2^{\,2} + 2a_1 a_2 \cos\phi \le (2d)^2 \tag{3}$$

The equations regulating the flow of an incompressible couple stress nanofluid [10,11] are presented as follows:

$$\frac{\partial U}{\partial X} + \frac{\partial V}{\partial Y} = 0 \tag{4}$$

$$\rho_f \left(\frac{\partial U}{\partial t'} + U\frac{\partial U}{\partial X} + V\frac{\partial U}{\partial Y} \right) = -\frac{\partial P}{\partial X} + \mu\left(\frac{\partial^2 U}{\partial X^2} + \frac{\partial^2 U}{\partial Y^2} \right) - \eta\left(\frac{\partial^4 U}{\partial X^4} + \frac{\partial^4 U}{\partial Y^4} \right) - \frac{\mu}{k_0}U$$
$$-\sigma' B_0^2 U + (1 - C_0)\rho_f g\beta_t (T - T_0) + (\rho_p - \rho_f) g\beta_t (C - C_0) \tag{5}$$

$$\rho_f \left(\frac{\partial V}{\partial t'} + U\frac{\partial V}{\partial X} + V\frac{\partial V}{\partial Y} \right) = -\frac{\partial P}{\partial Y} + \mu\left(\frac{\partial^2 V}{\partial X^2} + \frac{\partial^2 V}{\partial Y^2} \right) - \eta\left(\frac{\partial^4 V}{\partial X^4} + \frac{\partial^4 V}{\partial Y^4} \right) - \frac{\mu}{k_0}V \tag{6}$$

$$(\rho C')_f \left(\frac{\partial T}{\partial t'} + U\frac{\partial T}{\partial X} + V\frac{\partial T}{\partial Y} \right) = K\left(\frac{\partial^2 T}{\partial X^2} + \frac{\partial^2 T}{\partial Y^2} \right) + (\rho C')_p D_B \left(\frac{\partial C}{\partial X}\cdot\frac{\partial T}{\partial X} + \frac{\partial C}{\partial Y}\cdot\frac{\partial T}{\partial Y} \right) +$$
$$\frac{D_T (\rho C')_p}{T_m}\left(\left(\frac{\partial T}{\partial X} \right)^2 + \left(\frac{\partial T}{\partial Y} \right)^2 \right) + Q_0 - \frac{\partial q_r}{\partial Y} \tag{7}$$

$$\left(\frac{\partial C}{\partial t'} + U\frac{\partial C}{\partial X} + V\frac{\partial C}{\partial Y} \right) = D_B\left(\frac{\partial^2 C}{\partial X^2} + \frac{\partial^2 C}{\partial Y^2} \right) + \frac{D_B}{T_m}\left(\frac{\partial^2 T}{\partial X^2} + \frac{\partial^2 T}{\partial Y^2} \right) \tag{8}$$

Where $\partial/\partial t'$ is the material time derivative, (μ) is the coefficient of viscosity, *(P)* is the pressure in fixed frame, (η) denotes the constant related to couple stress, (k_0) represents the permeability parameter of the porous medium, (σ') signifies the electric conductivity coefficient, (B_0)indicates the transverse magnetic field, *(g)* refers to gravitational acceleration, $(\beta_t)$is the thermal expansion coefficient, $(\rho_f)$is the constant density of the base fluid, (ρ_p) is the density of the particle, *(T)* is the temperature of the fluid, (β_c) denotes the concentration expansion coefficient, (C'_f) the volumetric expansion coefficient is also referenced. *(K)* represents the thermal conductivity of the nanofluids, *(C)* denotes the nanoparticle concentration, (C'_p) is the specific heat at constant

pressure, (D_B) marks the Brownian diffusion coefficient, (T_m) refers to the fluid mean temperature, (D_T) signifies the thermophoretic diffusion coefficient, (Q_0) indicates the constant heat addition/absorption which may correspond to a thermal probe in biomedicine which creates a hot spot. In the mathematical model a Lorentzian magnetic drag force term appears which is characteristic of MHD pumping flows and acts transverse to the direction of the applied magnetic field. Here the Darcy-Brinkman model has been deployed which includes a linear drag force in the momentum equations for low Reynolds number propulsion. The radiative heat flux in the X – direction is negligible as compared to Y – direction but still represents physically achievable conditions in for example thermo-magnetic radiation therapy in biomedicine. Assuming the biofluid is optically thick, the Rosseland diffusion approximation for radiation hat transfer is valid and the associated radiative heat flux (q_r) is given by

$$q_r = -\frac{16\sigma^* T_0^3}{3k^*}.\frac{\partial T}{\partial Y} \tag{9}$$

Where (σ^*) and (k^*) are the Stefan-Boltzmann constant and mean absorption coefficient respectively.

In order to describe the fluid flow in the non-dimensional form, we introduce the following non dimensional quantities,

$$x=\frac{X}{\lambda}, y=\frac{Y}{d}, u=\frac{U}{c}, v=\frac{V}{c}, \delta=\frac{d}{\lambda}, t=\frac{ct}{\lambda}, h_1=\frac{H_1}{d}, h_2=\frac{H_2}{d}, a=\frac{a_1}{d}, b=\frac{a_2}{d}, m=\frac{\lambda m'}{d},$$

$$R=\frac{\rho_f cd}{\mu}, p=\frac{d^2P}{\mu c\lambda}, k=\frac{k_0}{d^2}, M^2=\frac{\sigma^* B_0^2 d^2}{\mu}, S^2=\frac{\mu d^2}{\eta}, \theta=\frac{T-T_0}{T_1-T_0}, \sigma=\frac{C-C_0}{C_1-C_0},$$

$$Gr=\frac{(1-C_0)\rho_f g\beta_c d^2(T_1-T_0)}{c\mu}, Br=\frac{(\rho_p-\rho_f)g\beta_c d^2(C_1-C_0)}{c\mu}, \Pr=\frac{C_f'\mu}{K},$$

$$\beta=\frac{d^2Q_0}{(T_1-T_0)\mu C_f'}, N_t=\frac{(T_1-T_0)D_T\rho_p C_p'}{T_m\mu C_f'}, N_b=\frac{(C_1-C_0)\rho_p C_p' D_B}{\mu C_f'}, Sc=\frac{\mu}{\rho_f D_B}, R_n=\frac{16\sigma^* T_0^3}{3k^*\mu C_f'}$$

Applying all non-dimensional quantities in governing equations (4) - (8) and introducing the stream function

$$u=\frac{\partial\psi}{\partial y}, v=-\delta\frac{\partial\psi}{\partial x}$$

The equations (5) – (8) expressed in terms of the stream function (ψ) are presented as follows,

$$R\delta\left(\frac{\partial}{\partial t}\left(\frac{\partial\psi}{\partial y}\right)+\frac{\partial\psi}{\partial y}\frac{\partial^2\psi}{\partial x\partial y}-\frac{\partial\psi}{\partial x}\frac{\partial^2\psi}{\partial y^2}\right)=-\frac{\partial p}{\partial x}+\left(\delta^2\frac{\partial^3\psi}{\partial x^2\partial y}+\frac{\partial^3\psi}{\partial y^3}\right)$$
$$-\frac{1}{S^2}\left(\delta^4\frac{\partial^5\psi}{\partial x^4\partial y}+\frac{\partial^5\psi}{\partial y^5}\right)-\left(\frac{1}{k}+M^2\right)\frac{\partial\psi}{\partial y}+Gr\theta+Br\sigma \tag{10}$$

$$R\delta^3\left(\frac{\partial}{\partial t}\left(\frac{\partial\psi}{\partial x}\right)+\frac{\partial\psi}{\partial y}\frac{\partial^2\psi}{\partial x^2}-\frac{\partial\psi}{\partial x}\frac{\partial^2\psi}{\partial x\partial y}\right)=\frac{\partial p}{\partial y}+\delta^2\left(\delta^2\frac{\partial^3\psi}{\partial x^3}+\frac{\partial^3\psi}{\partial x\partial y^2}\right)$$
$$-\frac{\delta^2}{S^2}\left(\delta^4\frac{\partial^5\psi}{\partial x^5}+\frac{\partial^5\psi}{\partial x\partial y^4}\right)-\frac{\delta^2}{k}\frac{\partial\psi}{\partial x} \tag{11}$$

$$R\delta\left(\frac{\partial\theta}{\partial t}+\frac{\partial\psi}{\partial y}\frac{\partial\theta}{\partial x}-\frac{\partial\psi}{\partial x}\frac{\partial\theta}{\partial y}\right)=\frac{1}{\mathrm{Pr}}\left(\delta^2\frac{\partial^2\theta}{\partial x^2}+\frac{\partial^2\theta}{\partial y^2}\right)+R_n\frac{\partial^2\theta}{\partial y^2}+N_b\left(\delta^2\frac{\partial\sigma}{\partial x}\frac{\partial\theta}{\partial x}+\frac{\partial\sigma}{\partial y}\frac{\partial\theta}{\partial y}\right)$$
$$+N_t\left(\delta^2\left(\frac{\partial\theta}{\partial x}\right)^2+\left(\frac{\partial\theta}{\partial y}\right)^2\right)+\beta \tag{12}$$

$$R\delta Sc\left(\frac{\partial\sigma}{\partial t}+\frac{\partial\psi}{\partial y}\frac{\partial\sigma}{\partial x}-\frac{\partial\psi}{\partial x}\frac{\partial\sigma}{\partial y}\right)=\left(\delta^2\frac{\partial^2\sigma}{\partial x^2}+\frac{\partial^2\sigma}{\partial y^2}\right)+\frac{N_t}{N_b}\left(\delta^2\frac{\partial^2\theta}{\partial x^2}+\frac{\partial^2\theta}{\partial y^2}\right) \tag{13}$$

Where *(t)* is the dimensionless time, *(x)* is the dimensionless axial coordinate, *(y)* is the dimensionless transverse coordinate, *(u)* and *(v)* are dimensionless axial and transverse velocity components, *(p)* is the dimensionless pressure, *(R)* is the Reynolds number, (δ) is the wave number, *(M)* is the Hartmann number, *(k)* is the porosity parameter, (θ) is the dimensionless temperature, (σ) is the dimensionless rescaled nanoparticle volume fraction, *(Pr)* is the Prandtl number, *(Gr)* is the local Grashof number, *(Br)* is the local nanoparticle Grashof number, (N_b) is the Brownian motion parameter, (N_t) is the thermophoresis parameter, (R_n) is the radiation parameter, (β) is the non-dimensional heat source/sink parameter and *(Sc)* is the Schmidt number. Reducing all the equations under long wavelength and low Reynolds number approximation, and neglecting the first and higher order of (δ), the Eqs. (10) – (13) become,

$$0=-\frac{\partial p}{\partial x}+\frac{\partial^3\psi}{\partial y^3}-\frac{1}{S^2}\frac{\partial^5\psi}{\partial y^5}-H^2\frac{\partial\psi}{\partial y}+Gr\theta+Br\sigma \tag{14}$$

$$0=\frac{\partial p}{\partial y} \tag{15}$$

$$0=\xi\frac{\partial^2\theta}{\partial y^2}+N_b\frac{\partial\sigma}{\partial y}\frac{\partial\theta}{\partial y}+N_t\left(\frac{\partial\theta}{\partial y}\right)^2+\beta \tag{16}$$

$$0=\frac{\partial^2\sigma}{\partial y^2}+\frac{N_t}{N_b}\frac{\partial^2\theta}{\partial y^2} \tag{17}$$

Eliminating of pressure term from Eqs. (14) and (15) gives,

$$\frac{\partial^4 \psi}{\partial y^4} - \frac{1}{S^2}\frac{\partial^6 \psi}{\partial y^6} - H^2\frac{\partial^2 \psi}{\partial y^2} + Gr\frac{\partial \theta}{\partial y} + Br\frac{\partial \sigma}{\partial y} = 0 \tag{18}$$

$$\xi\frac{\partial^2 \theta}{\partial y^2} + N_b\frac{\partial \sigma}{\partial y}\frac{\partial \theta}{\partial y} + N_t\left(\frac{\partial \theta}{\partial y}\right)^2 + \beta = 0 \tag{19}$$

$$\frac{\partial^2 \sigma}{\partial y^2} + \frac{N_t}{N_b}\frac{\partial^2 \theta}{\partial y^2} = 0 \tag{20}$$

where $\xi = \dfrac{1+\Pr R_n}{\Pr}$ (21)

The corresponding boundary conditions in terms of stream function are given by [2, 5, 13],

$$\psi = -\frac{F}{2}, \frac{\partial \psi}{\partial y} = -L\frac{\partial^2 \psi}{\partial y^2}, \theta + \gamma\frac{\partial \theta}{\partial y} = 0, \sigma + \gamma_1\frac{\partial \sigma}{\partial y} = 0 \qquad \text{at} \quad y = h_1 \tag{22}$$

$$\psi = \frac{F}{2}, \frac{\partial \psi}{\partial y} = L\frac{\partial^2 \psi}{\partial y^2}, \theta - \gamma\frac{\partial \theta}{\partial y} = 1, \sigma - \gamma_1\frac{\partial \sigma}{\partial y} = 1 \qquad \text{at} \quad y = h_2 \tag{23}$$

$$h_1(x,t) = 1 + mx + a\sin 2\pi(x-t), h_2(x,t) = -1 - mx - b\sin\left(2\pi(x-t) + \phi\right) \tag{24}$$

Where *(a)* and *(b)* are the amplitudes of left and right walls respectively, *(m)* is the non - uniform parameter, *(F)* is the flux in the wave frame and *(a)*, *(b)*, (ϕ) and *(d)* satisfies the relation:

$$a^2 + b^2 + 2ab\cos\phi \le (2d)^2 \tag{25}$$

The time averaged flow over a period at a fixed position X is defined as

$$\bar{Q} = \frac{1}{T}\int_0^T Q dt' \tag{26}$$

We find

$$\bar{Q} = q + a_1 c\sin\frac{2\pi}{\lambda}(X - ct') + a_2 c\sin\left[\frac{2\pi}{\lambda}(X - ct') + \phi\right] \tag{27}$$

$$q = \int_{H_2}^{H_1} u(x,y)dy \tag{28}$$

Where *(q)* is the rate of volume flow in the moving frame.

If we find dimensionless mean flows *(F)*, in the laboratory frame and (Θ) in the wave frame to

$$\Theta = \frac{\bar{Q}}{cd}, F = \frac{q}{cd} \tag{29}$$

Where (Θ) is the time average of the flux over one period of the wave and *(F)* is the flux.

After using non dimensional quantities in Eq. (29), it is found that Eq. (27) becomes [13, 14, 19, 24],

$$F(x,t)=\Theta+a\sin 2\pi(x-t)+b\sin\left(2\pi(x-t)+\phi\right) \tag{30}$$

In which,

$$F=\int_{h_2}^{h_1} u\,dy \tag{31}$$

3. Exact analytical solution of the problem

Solving the Eqns. (18) - (20) subject to the boundary conditions (22) and (23), the temperature, concentration and and stream function solutions are determined as follows:

$$\theta=c_1+c_2e^{-f_2y}-\frac{\beta y}{\xi f_2} \tag{32}$$

$$\sigma=-\frac{N_t}{N_b}c_2e^{-f_2y}+c_3y+c_4 \tag{33}$$

$$\psi=c_5+c_6y+c_7\cosh Ay+c_8\sinh Ay+c_9\cosh By+c_{10}\sinh By+f_8y^2+f_7e^{-f_2y} \tag{34}$$

f_1 is obtained by assuming $\gamma=\gamma_1$ (i.e. by assuming the slip parameters of temperature and concentration are equal),

Where $f_1=\dfrac{N_t+N_b}{N_b(h_2-h_1-2\gamma_1)}$, $f_2=\dfrac{N_bf_1}{\xi}$

The mathematical expression for axial velocity is derived from Equation (34).

$$u=c_6+c_7A\sinh Ay+c_8A\cosh Ay+c_9B\sinh By+c_{10}B\cosh By+2f_8y-f_7f_2e^{-f_2y} \tag{35}$$

The expression for pressure gradient is obtained from Eq. (14),

$$\frac{dp}{dx}=f_9\sinh Ay+f_{10}\cosh Ay+f_{11}\sinh By+f_{12}\cosh By+f_{13}e^{-f_2y}+f_{14}y+f_{15} \tag{36}$$

Where $A=\dfrac{1}{\sqrt{2}}\left[\sqrt{S^2+S\sqrt{S^2-4H^2}}\right]$, $B=\dfrac{1}{\sqrt{2}}\left[\sqrt{S^2-S\sqrt{S^2-4H^2}}\right]$ and $H^2=M^2+\dfrac{1}{k}$

The non-dimensional form for the heat transfer coefficient *(Z)* and the pressure rise (ΔP) is expressed as follows:

$$Z=h_{2x}\theta_y \tag{37}$$

$$\Delta P = \int_0^1 \int_0^1 \left(\frac{\partial p}{\partial x} \right)_{y=0} dxdt \tag{38}$$

4. Results and Discussion

The pressure gradient (dP/dx), velocity *(u)*, temperature *(θ)*, concentration *(σ)*, and streamlines *(ψ)* of the couple stress nanofluid model are examined by numerical and graphical methods. The impact of several parameters, including the Hartmann magnetic number *(M)*, Prandtl number *(Pr)*, heat source/sink parameter *(β)*, Grashof number *(Gr)*, nanoparticle Grashof number *(Br)*, Brownian motion parameter (N_b), thermophoresis parameter (N_t), radiation parameter (R_n), couple stress parameter *(S)*, slip parameter *(L)*, and non-uniform parameter *(m)* on axial velocity, pressure gradient, temperature, concentration, heat transfer coefficient, and average pressure rise is illustrated in **Figs. 2–29.**

4.1 Velocity distribution

The variation of fluid parameters related to axial velocity *(u)* is thoroughly illustrated in **Figs. 2–7**, demonstrating that the velocity profiles possess a parabolic nature. Each graph elucidates how various fluid dynamic parameters affect the velocity distribution within the channel, enhancing an appreciation of the key transport phenomena of relevance to medical applications. The influence of the Hartmann number *(M)* on the velocity *(u)* is analyzed from **Fig. 2**. The graph indicates that an increase in the Hartmann number correlates with a significant rise in velocity near the channel walls. This phenomenon arises from the magnetic field effect, which diminishes velocity at the channel center (core zone) while augmenting it around the walls, associated with a re-distribution in linear momentum. Conversely, in the central region of the channel, an increase in *(M)* leads to a reduction in velocity. This phenomenon indicates a non-uniform interaction between the magnetic field and the fluid flow, resulting in varied velocity over the channel's cross-section. **Fig. 3** displayed the influence of the couple stress parameter *(S)* on the velocity field. The results indicate a complex interaction in which an increase in *(S)* correlates with an elevation in velocity in specific portions of the channel, whereas in other areas, the velocity diminishes. In specific places, this resistance may produce a more uniform velocity distribution, perhaps enhancing flow velocity near the centre of the domain, particularly in shear-driven flows within channels. The dual effect is likely attributable to the impact of couple tensions, which generate resistance in certain regions while facilitating flow in others. **Fig. 4** analyzes the influence of the thermophoresis

parameter (N_t) on velocity. Analogous to the couple stress parameter, an increase in (N_t) results in an elevation in velocity in certain regions and a reduction in others. Thermophoresis, the movement of particles induced by temperature gradients, results in variations in flow patterns, with increased particle motion in areas of elevated temperature gradients. **Fig. 5** emphasizes the impact of the slip parameter *(L)* on velocity profiles. It is evident that the slip parameter influences velocity in a manner akin to the non-Newtonian couple stress parameter *(S)*. Both characteristics exert alternating influences on velocity, resulting in areas of both enhanced and diminished flow. This indicates that the slip at the channel barrier intricately influences the velocity distribution, contingent upon the particular area within the channel. This greater slip parameter results in a more pronounced effect of the velocity gradient near the surface, causing acceleration of the fluid in that specific region. A similar behavior of the slip parameter has been observed in the findings of Shankar et al. [28]. The local Grashof number *(Gr)*, indicating the ratio of buoyancy to viscous forces, significantly influences velocity, as explored in **Fig. 6**. In the region $-h_2 < y < 0.4$, the velocity escalates with an increase in *(Gr)*, propelled by buoyant forces. In the interval $0.4 < y < h_1$, the velocity diminishes, signifying that viscous forces prevail over buoyancy, resulting in a divergent impact on flow dynamics. **Fig. 7** illustrates the impact of the nanoparticle Grashof number *(Br)*, which quantifies the buoyancy effect resulting from the concentration gradients of nanoparticles. Analogous to the (N_t) thermophoresis parameter, *(Br)* exhibits an increase in velocity in certain locations while demonstrating a decrease in others. This indicates that differences in nanoparticle concentration substantially affect fluid dynamics and velocity distribution inside the channel.

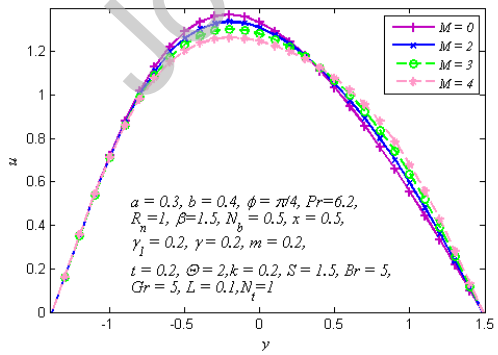

Fig. 2 Velocity profile *(u)* for *(M)*

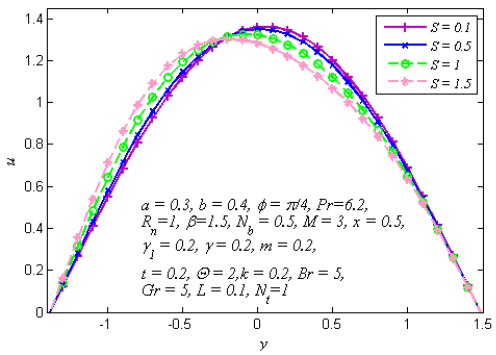

Fig. 3 Velocity profile *(u)* for *(S)*

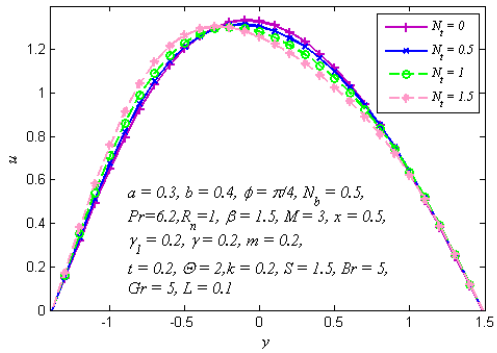

Fig. 4 Velocity profile *(u)* for (N_t)

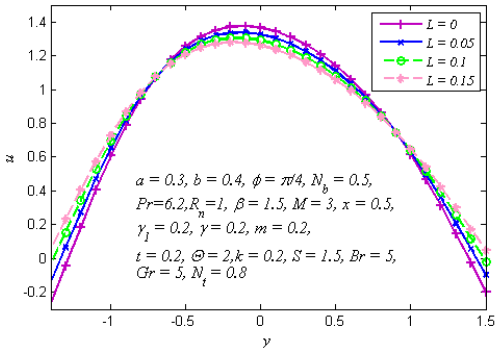

Fig. 5 Velocity profile *(u)* for *(L)*

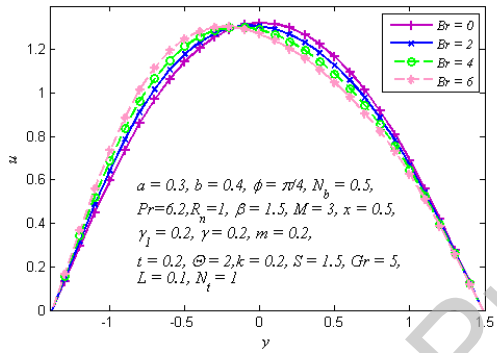

Fig. 6 Velocity profile *(u)* for *(Br)*

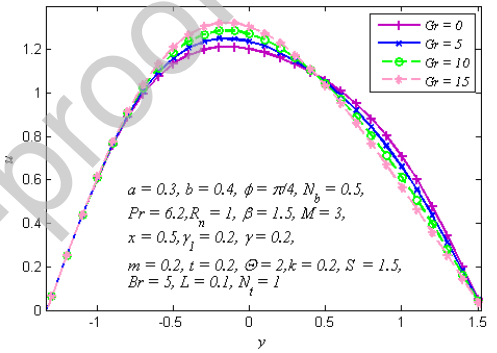

Fig. 7 Velocity profile *(u)* for *(Gr)*

Figures 8 to 11 are illustrated to examine the influence of different physical parameters on the pressure gradient across one wavelength period (0,1). **Figs. 8 and 9** indicate that the pressure gradient decreases with the increase in permeability of the porous medium *(k)* and couple stress parameter *(S)*. With an increase in permeability, i.e. progressive depletion of obstructive material in the conduit (channel), the fluid encounters less drag and resistance from the porous medium solid fibers, hence reducing the requirement for a substantial pressure gradient to sustain the same flow rate. An elevation in *(S)* introduces supplementary shear resistance due to the fluid's microstructural interactions. This diminishes the velocity gradient in high-shear areas, resulting in a smaller pressure gradient. **Fig. 10** presents the effect of phase difference (ϕ) on the pressure gradient. It is noted that the pressure gradient decreases in both the wide and the narrow part of the channel. Furthermore, it is observed that the narrow region in the channel shifts to the left with an increase in phase shift (ϕ). **Fig. 11** clearly shows that an increase in thermophoresis parameter

(N_t) results in an increase in the amplitude of the pressure gradient. As (N_t) grows, the thermophoretic force exerted on particles intensifies, resulting in enhanced migration of particles towards cooler areas. This redistribution locally modifies the fluid density and viscosity, potentially resulting in fluctuations in the pressure necessary to maintain the flow.

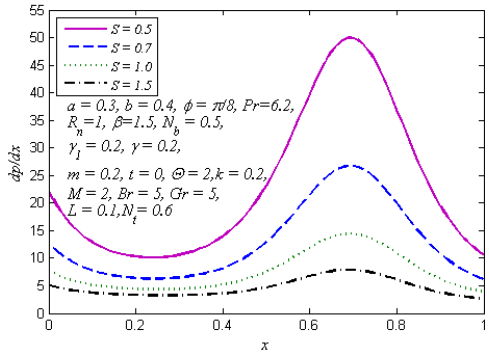

Fig. 8 Pressure Gradient profile (dp/dx) for *(S)*

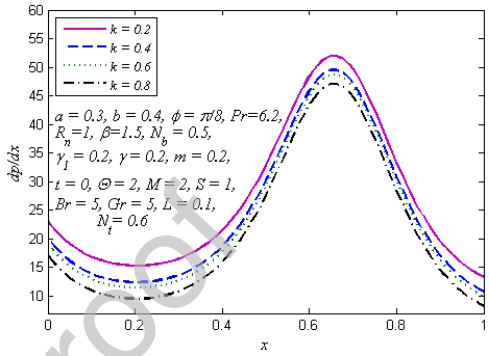

Fig. 9 Pressure Gradient profile (dp/dx) for *(k)*

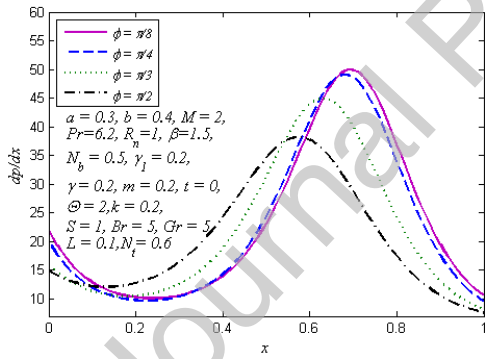

Fig. 10 Pressure Gradient profile (dp/dx) for (ϕ)

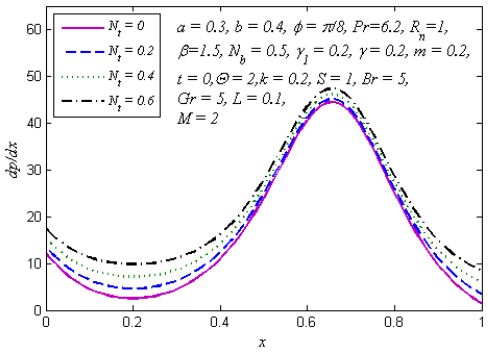

Fig. 11 Pressure Gradient profile (dp/dx) for (N_t)

4.2 Temperature distribution

Figs 12 - 15 analysis investigates the temperature profiles for different values of the slip parameter (γ), radiation parameter (R_n), Brownian motion parameter (N_b), and Prandtl number *(Pr)*. **Fig.**

12 illustrates and examines the influence of the radiation parameter (R_n) on the fluid temperature. We observe that a rise in (R_n) leads to a decrease in fluid temperature. The inverse connection arises from increased radiative heat transfer, which facilitates energy dissipation from the fluid and reduces the temperature. The fluid dissipates additional energy as (R_n) increases, thereby diminishing the internal thermal energy. **Fig. 13** illustrates that as (γ) (slip parameter) escalates, the temperature concurrently climbs, presumably due to less frictional resistance at the interfaces, facilitating enhanced heat accumulation within the fluid. **Fig. 14** illustrates the temperature profile for different Prandtl number *(Pr)* values. The Prandtl number denotes the ratio of momentum diffusivity to thermal diffusivity, with distinct fluids exhibiting various Pr values. The graphic indicates that when the Prandtl number *(Pr)* increases—from 0.015 for mercury, 0.71 for air, 7 for water, to 11.2 for water at 4°C the temperature of the fluid rises. Lower Prandtl numbers, such as those associated with mercury, demonstrate a linear temperature distribution, whereas higher Prandtl numbers, like those for water, display a parabolic distribution. This transition signifies that when *(Pr)* increases, the thermal conductivity of the fluid diminishes, resulting in more pronounced temperature gradients within the flow. **Fig. 15** illustrates that an elevation in the Brownian motion parameter (N_b) corresponds with an increase in temperature. Similarly, Bilal et al. [38,39] emphasized that an increase in the Brownian motion parameter (N_b) intensifies the temperature distribution, as a higher concentration of particles enhances thermophoretic activity. Brownian motion is accelerated by the heat energy of fluid molecules. As the temperature escalates, the kinetic energy of these molecules correspondingly increases, resulting in more intense and frequent collisions with suspended particles. This increased activity leads to a rise in the fluid's temperature.

4.3 Concentration Distribution

Figs. 16–19 show how the nanofluid's concentration changes with different parameters. They show how the heat source/sink parameter (β), non-uniform parameter *(m)*, thermophoresis parameter (N_t) and Brownian motion parameter (N_b) affect the concentration of nanoparticles. In **Fig. 16**, an increase in (β) (heat source) diminishes the concentration. As (β) grows, the heat

source produces supplementary thermal energy within the system, amplifying temperature gradients. These gradients can induce solutes or particles to migrate from areas of elevated temperature due to thermal diffusion or thermophoretic processes. **Fig. 17** demonstrates that increased non-uniformity *(m)* leads to a diminished nanoparticle concentration, suggesting that irregular flow patterns induced by non-uniformity distribute particles more uniformly, hence decreasing local concentrations. **Fig. 18** illustrates that a variation in the thermophoresis parameter (N_t). Enhanced (N_t) facilitates the temperature-dependent diffusion of particles. This phenomenon disperses the particles throughout a wider area, reducing their concentration, especially in areas of elevated temperature. A more pronounced thermophoretic effect results in a greater decrease in concentration adjacent to the heat source or in areas of increased temperature. **Fig. 19** shows that as the amount of (N_b) goes up, the concentration goes up too. This is because increased Brownian motion causes more random particle movement, which leads to more nanoparticles building up in the fluid. The Brownian motion parameter (N_b) indicates the magnitude of random, thermally induced particle movement in a fluid. As (N_b) increases, the kinetic energy of the particles escalates, resulting in more intense motion. This improved mobility facilitates improved mixing and diminishes the probability of particle sedimentation, thereby elevating the total concentration of particles in the fluid.

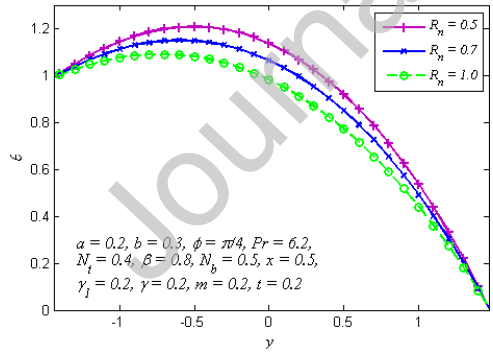

Fig. 12 Temperature profile (θ) for (R_n)

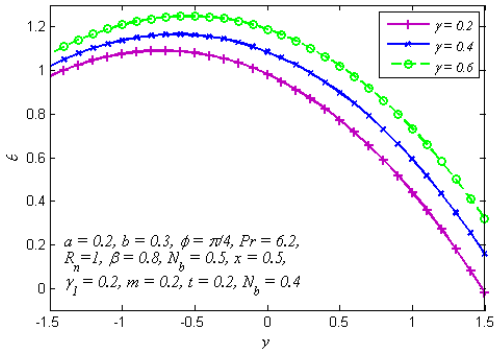

Fig. 13 Temperature profile (θ) for (γ)

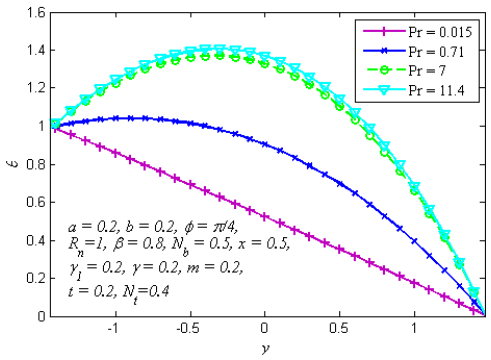

Fig. 14 Temperature profile (θ) for *(Pr)*

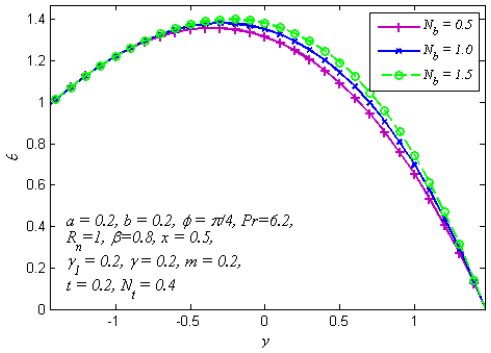

Fig. 15 Temperature profile (θ) for (N_b)

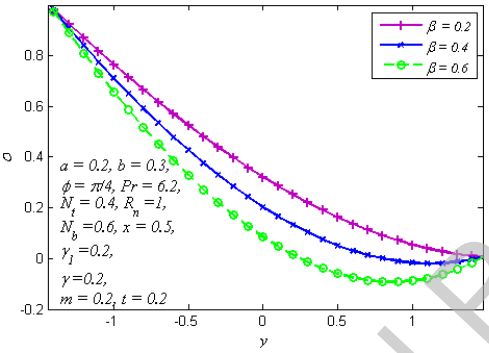

Fig. 16 Concentration profile (σ) for (β)

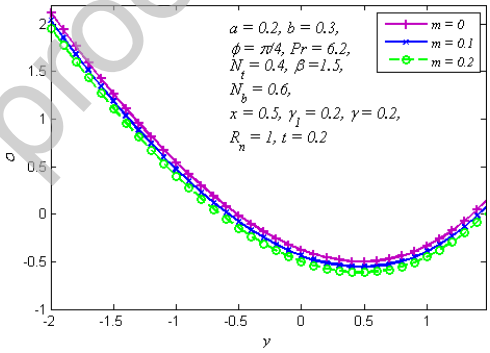

Fig. 17 Concentration profile (σ) for *(m)*

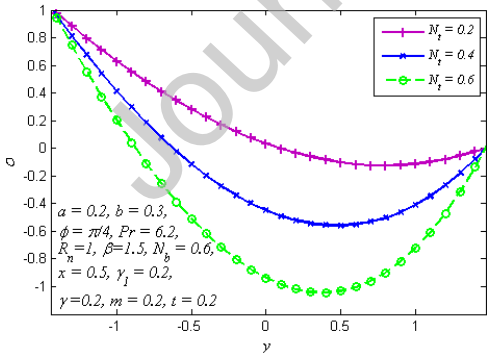

Fig. 18 Concentration profile (σ) for (N_t)

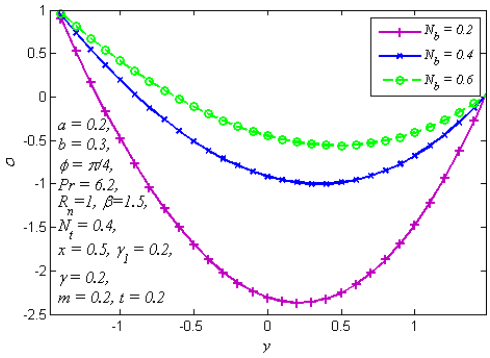

Fig. 19 Concentration profile (σ) for (N_b)

4.4 The heat transfer coefficient

Figs 20–23 depict the behavior of the heat transfer coefficient *(Z)* in relation to diverse physical characteristics, elucidating the impact of these parameters on heat transfer efficiency within the fluid system. The data indicate that the heat transfer coefficient displays oscillatory behavior because of the contraction and expansion of the channel walls, a crucial aspect influencing heat transport within the system. **Fig. 20** analyzes the influence of the heat source/sink parameter (β) on the heat transfer coefficient *(Z)*. It indicates that as (β) rises, *(Z)* also ascends. A more potent heat source results in increased heat generation inside the fluid, hence augmenting the total rate of heat transfer. This suggests that elevated (β) values enhance heat transmission by augmenting the thermal energy present in the system. **Fig. 21** illustrates the effect of the radiation parameter (R_n) on *(Z)*. In contrast to the other factors, a rise in (R_n) results in a reduction in the heat transfer coefficient. Radiation promotes energy absorption in the system, resulting in accelerated fluid cooling at the boundary of the conduit (channel) and consequently diminishing the heat available for transfer. The efficiency of heat transmission diminishes with increased radiation levels, resulting in a fall in *(Z)*. **Fig. 22** illustrates the effect of the slip parameter (γ) on the heat transfer coefficient. An elevation in (γ) leads to an augmentation in *(Z)*. The slip parameter diminishes the friction between the fluid and the channel walls, facilitating smoother fluid flow and decreasing thermal resistance. This enhances the efficiency of heat movement along the channel, resulting in an elevated heat transfer coefficient. **Fig. 23** illustrates the effect of the Prandtl number *(Pr)* on the heat transfer coefficient. As *(Pr)* rises, *(Z)* also ascends. Elevated Prandtl numbers are indicative of fluids with less thermal diffusivity (like water), which retain heat inside the fluid and improve the heat transmission mechanism. This results in a more effective heat exchange and an elevated value of *(Z)* as *(Pr)* increases.

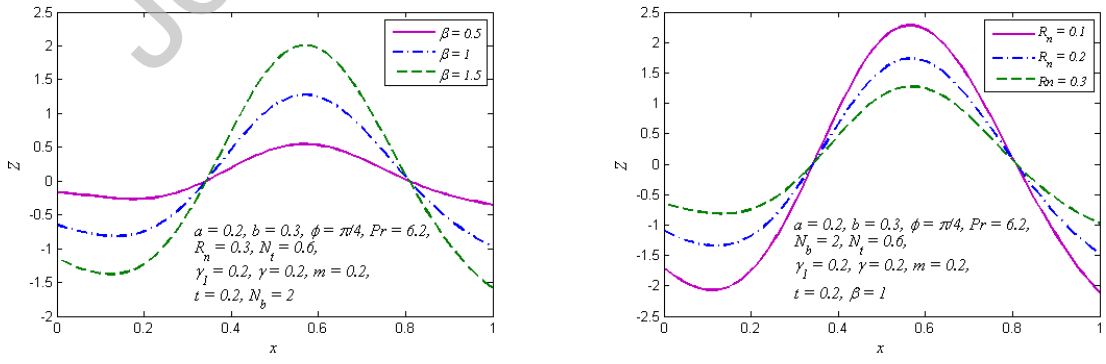

Fig. 20 Coefficient of heat transfer *(Z)* for (β)

Fig. 21 Coefficient of heat transfer *(Z)* for (R_n)

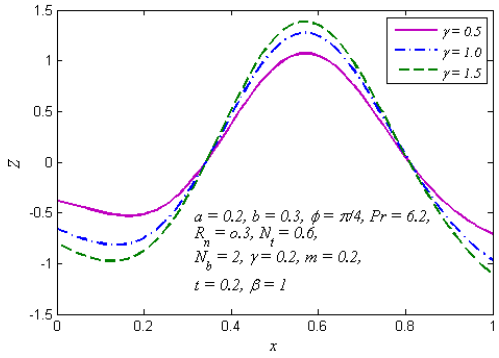

Fig. 22 Coefficient of heat transfer *(Z)* for (γ)

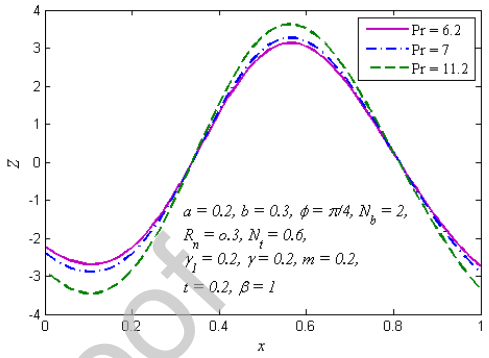

Fig. 23 Coefficient of heat transfer *(Z)* for *(Pr)*

4.5 Pressure drop

The correlation between the average pressure rise (ΔP) and the time-averaged flow rate (Θ) for several parameter values, including the non-uniform parameter *(m)*, Hartmann number *(M)*, slip parameter *(L)*, and Grashof number *(Gr)*, is computed and illustrated in Figs. 42–45. The complete flow zone is categorized into four quadrants according to the signs of (ΔP) and (Θ), each indicating a distinct flow behavior:

- Quadrant I ($\Delta P > 0$, $\Theta > 0$) pertains to the peristaltic pumping zone, characterized by positive pressure increase and flow rate.
- Quadrant II ($\Delta P < 0$, $\Theta > 0$) represents the increased flow zone, wherein the pressure decline facilitates the positive flow rate.
- Quadrant III, the free pumping area is defined by $\Delta P = 0$, where the positive flow (Q > 0) is solely attributed to peristalsis, compensating for the lack of a pressure differential.
- Quadrant IV ($\Delta P > 0$, $\Theta < 0$) represents the retrograde pumping zone, characterized by flow moving in the opposite direction despite an increase in pressure.

Each picture illustrates the influence of various physical characteristics on the interaction between (ΔP) and (Θ) in these locations.

Fig. 24 depicts the correlation between the average pressure increase (ΔP) and the time-averaged flow rate (Θ) for different values of the Hartmann number *(M)*. As *(M)* grows, the correlation between (ΔP) and (Θ) exhibits greater linearity, signifying a more direct connection between pressure rise and flow rate. Moreover, an elevation in M augments peristaltic pumping in quadrant I, as the magnetic field (denoted by *(M)*) heightens the barrier to fluid movement, necessitating a bigger pressure increase for an equivalent flow rate. This leads to enhanced peristaltic pumping as *(M)* increases. **Fig. 25** illustrates the impact of the non-uniform parameter *(m)* on (ΔP) and (Θ). It is noted that an increase in m results in improved peristaltic pumping throughout the expanded flow zone (quadrant II). This indicates that channel non-uniformity enhances the fluid's capacity to flow in reaction to the pressure differential. As *(m)* grows, the system demonstrates enhanced fluid transport efficiency, leading to elevated flow rates for a specified pressure increase. This phenomenon is especially evident in the augmented flow zone, where (ΔP) is negative but the flow rate persists as positive. An analogous trend in analysis [29] reveals a linear relationship between (ΔP) and (Θ), where for larger values of M, the observed trends are inverse to those of m in both cases when $(\Delta P) > 0$ and $(\Delta P) < 0$. **Fig. 26** examines the influence of the slip parameter *(L)* on the correlation between (ΔP) and (Θ). The findings indicate that as *(L)* increases, peristaltic pumping diminishes in all areas. An increased slip parameter diminishes the friction between the fluid and the channel walls, facilitating enhanced fluid motion with a lower requisite pressure increase. The reduction in the necessary pressure for a specific flow rate leads to less peristaltic pumping, especially in quadrant I, where both (ΔP) and (Θ) are positive. The impact of the Grashof number *(Gr)* on (ΔP) and (Θ) is depicted with variations in **Fig. 27**. An increase in *(Gr)* correlates with enhanced pumping throughout all quadrants. The Grashof number denotes the ratio of buoyant forces to viscous forces, and as *(Gr)* grows, buoyant effects become increasingly predominant. This leads to enhanced fluid dynamics for a certain pressure increase, hence improving peristaltic pumping universally. Quadrant I exhibit a significant enhancement in peristaltic pumping with elevated *(Gr)*, as buoyant forces facilitate fluid motion more efficiently.

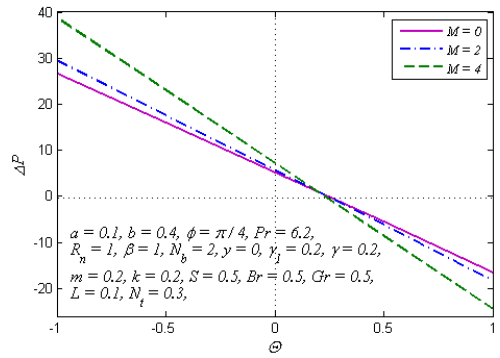

Fig. 24 Average pressure rise (ΔP) for *(M)*

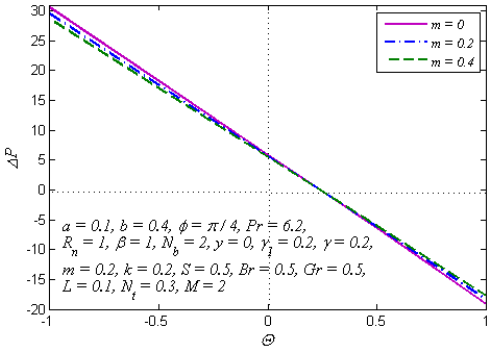

Fig. 25 Average pressure rise (ΔP) for *(m)*

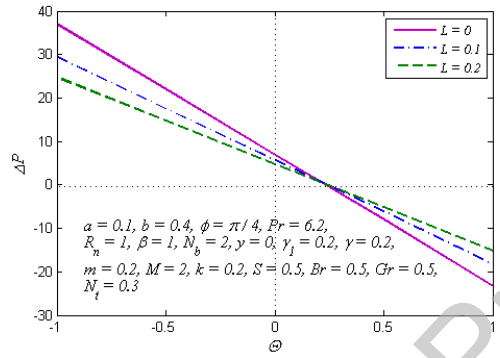

Fig. 26 Average pressure rise (ΔP) for *(L)*

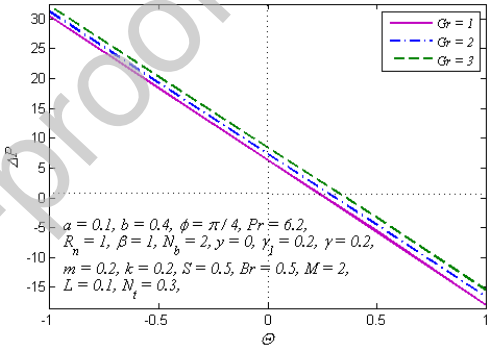

Fig. 27 Average pressure rise (ΔP) for *(Gr)*

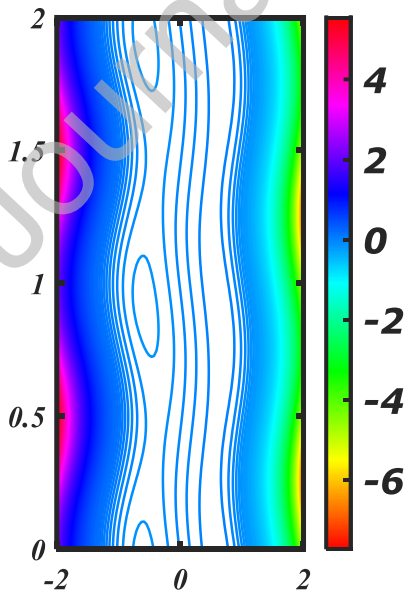

a) S = 3

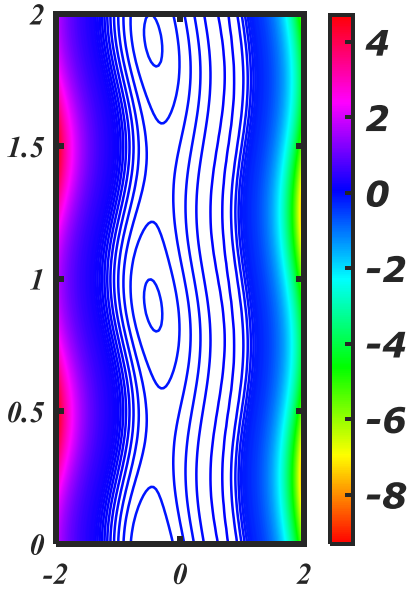

b) S = 5

Fig. 28 Streamline plot for varying couple stress parameter *(S)* (a) $S = 3$, (b) $S = 5$

4.6 Streamline plots

In peristaltic motion, a prominent phenomenon known as "trapping" occurs, characterized by fluid boluses constrained within specific regions of the flow. These boluses, observed in streamline patterns, represent portions of the couple stress fluid moving at the wave speed, as if they are "captured" by the peristaltic waves propagating along the deformable microchannel walls. Trapping typically arises under specific conditions, notably when the amplitude ratio is large. This phenomenon has been examined for various values of the couple stress parameter *(S)* and porosity parameter *(k)* in the context of couple stress nanofluid flow within a tapered, magnetised porous channel. The results, depicted in **Figs. 28 and 29**, highlight the influence of these parameters on the trapping mechanism and the behaviour of boluses in this specific flow configuration. **Fig. 28** explains the couple stress parameter *(S)* escalates, boluses in the streamline plots enlarge, manifesting as more substantial recirculatory zones. These boluses may additionally migrate deeper into the domain due to increased rotating effects. In systems involving couple stress fluids, larger boluses can enhance heat and mass transfer by increasing the recirculation of the fluid, improving overall system performance. **Fig. 29** depicts the streamline variation with varying values of porosity parameter *(k)*. As porosity rises, the fluid's contact with the porous material diminishes shear forces that frequently contribute to bolus development. The diminished strength of secondary flow immediately constrains the magnitude and intensity of recirculatory zones.

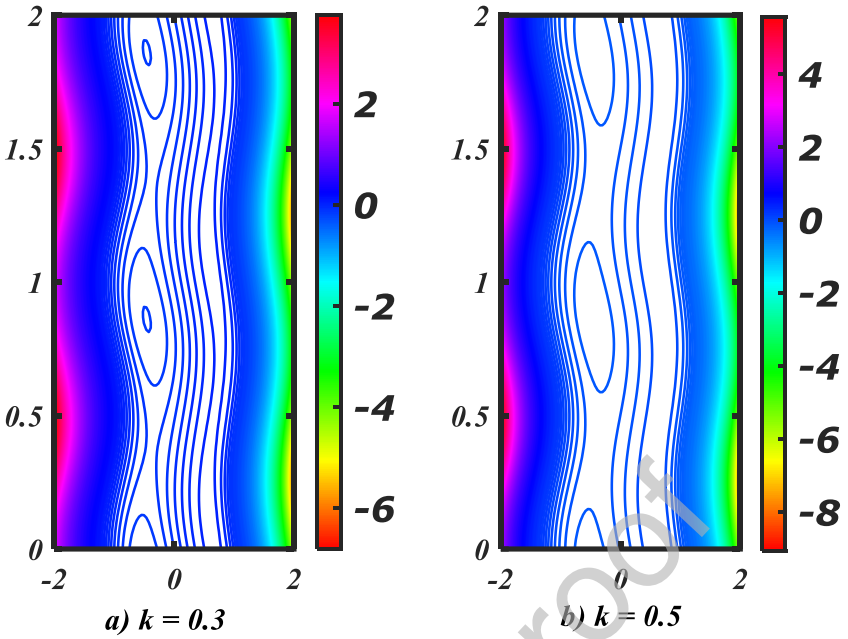

Fig. 29 Streamline plot for varying *(k)* porosity parameter (a) $k = 0.3$, (b) $k = 0.5$

Conclusions

The current study, motivated by applications in nano-drug transport in the gastric tract and biomagnetic thermal radiation therapy, has investigated the peristaltic motion of a magnetohydrodynamic (MHD) couple stress nanofluid in a tapered asymmetric channel containing a non-deformable porous medium with slip effects and radiative heat transfer. The governing equations for the couple stress nanofluid are simplified by employing long wavelength and low Reynolds number approximations, enabling the linearisation of the equations. Analytical solutions for key flow variables including velocity, pressure gradient, temperature, nanoparticle concentration profiles, and the heat transfer coefficient were produced and examined through graphical representations. The principal conclusions are as follows:

(i) Velocity is elevated i.e. flow acceleration is produced with increasing values of the Brownian motion parameter (N_b), non-uniform parameter (m), and slip parameter (L). These factors improve

fluid dynamics by facilitating nanoparticle movement and diminishing boundary resistance. The velocity diminishes as the Hartmann number (M) and Grashof number (Gr) increase.

(ii) Stronger magnetic field (M) produces a Lorentz force that inhibits flow i.e. induces core zone flow deceleration, whilst thermal buoyancy effects (Gr) diminish fluid velocity adjacent to the channel walls.

(iii) The pressure gradient is elevated with the Hartmann number (M) and the slip parameter (L). An intensified magnetic field increases resistance to fluid motion, necessitating a greater pressure gradient, whereas augmented slip at the boundaries diminishes friction, also demanding a larger pressure gradient to maintain flow.

(iv) Temperature increases with the elevation of both the thermophoresis parameter (N_t) and the Brownian motion parameter (N_b). These factors facilitate the heat transfer process by propelling particles from hotter to cooler areas (N_t) and inducing random thermal motion (N_b), both of which increase the fluid's total temperature.

(v) Nanoparticle concentration magnitudes exhibit a declining tendency with increases in the heat source parameter (β), slip parameter (γ), non-uniform parameter (m), thermophoresis parameter (N_t), and Prandtl number (Pr). These parameters enhance nanoparticle diffusion, hence diminishing local concentrations. The concentration profile is enhanced with thermal radiation parameter (R_n), as radiative effects lead to energy accumulation which influences nanoparticle diffusion.

(vi) The heat transfer coefficient (Z) rises with the heat source parameter (β), non-uniform parameter (m), thermophoresis parameter (N_t), Brownian motion parameter (N_b), and Prandtl number (Pr). These parameters augment thermal conductivity and energy transmission within the system, resulting in an increased rate of heat transfer to the walls of the conduit.

(vii) Pumping efficiency is more effective in a uniform channel than in a non-uniform channel. Non-uniformity engenders flow resistance and anomalies in the pumping transport, hence diminishing the efficacy of peristaltic pumping systems. A homogeneous channel facilitates smoother fluid movement, resulting in enhanced pumping efficiency.

This paper offers an extensive examination of peristaltic transport in a magnetohydrodynamic couple stress nanofluid as a model of nano-drug transport in the gastric tract, and features many factors, such as magnetic fields, thermophoresis, Brownian motion, and slip effects. The results

illustrate the crucial influence of these factors on regulating fluid velocity, temperature, nanoparticle concentration, pressure, and heat transfer within the system. These multi-physical aspects when considered simultaneously provide a more generalized appraisal of actual thermo-magnetic radiation and nano-drug applications, enabling a deeper understanding of the interplay of multiple effects on pumping efficiency. The analytical answers and insights obtained can inform the design of more efficient systems for heat transfer, medication delivery, and other fluidic processes. Future studies may address 3-D pumping, alternate non-Newtonian models e.g. Eringen's micropolar model (which includes angular momentum of suspended particles), alternative radiative flux models e.g. Schuster-Schwarzchild two-flux model and additionally may consider non-Darcy inertial (Forchheimer) effects for porous media.

CRediT authorship contribution statement

P. Deepalakshmi: Writing – original draft, Conceptualization, **G. Shankar:** Writing – review & editing, Methodology, **E.P. Siva:** Visualization, Supervision, Investigation, **D. Tripathi:** Validation, Formal analysis, **O. Anwar Beg:** Data curation. Writing – review & editing

Declaration of competing interest

The authors declare that they have no known competing financial interests or personal relationships that could have appeared to influence the work reported in this paper.

Data availability

Data will be made available on request.

Nomenclature

X,Y	Laboratory reference frame	γ	Slip parameter
x,y	Wave frame of reference	μ	Fluid dynamic viscosity
S	Couple stress fluid	K	Thermal conductivity

H_1, H_2	Upper and lower channel walls	ρ_f, ρ_p	Density of the base fluid and particle
d_1, d_2	Half-width of the microchannel	β_t, β_c	Thermal and concentration expansion coefficient
a_1, b_1	Wave amplitude	σ'	Electric conductivity coefficient
T_0, T_1	Wall Temperature	k^*	Rosseland mean absorption coefficient
t	Time period	C	Nanoparticle concentration
λ	Wavelength	C'_p	Specific heat at constant pressure
c	Wave velocity	N_b	Brownian diffusion coefficient
B_0	Uniform magnetic field	N_t	Thermophoresis parameter
ϕ	Phase difference	R	Reynolds number
T	Temperature of the fluid	M	Hartmann number
P	Pressure of the liquid	k	Porous parameter
g	The acceleration caused by gravity	Gr	Thermal grashof number
Q_0	Heat addition/absorption	Sc	Schmidt number
k_0	Permeability of a porous medium	R_n	Radiation parameter
q_r	Radiation heat flux	Pr	Prandtl number
m	Non-uniform parameter	Br	Local nanoparticle Grashof number

References

1) T.W.Latham, Fluid motion in Peristaltic pump, MS Thesis (1966) MIT Cambridge.

2) A.H.Shapiro and M.Y.Jaffrin, Peristaltic pumping with long wavelength at low Reynolds number, Weinberg J. Fluid Mech. **37** (1969) 799-825.
3) G.Radhakrishnamacharya and V.Radhakrishna Murty, Heat transfer to peristaltic transport in a non-uniform channel, Def. Sci. J. **43** (1993) 275-280.
4) B.B.Gupta and V.Sheshadri, Peristaltic pumping in non-uniform tubes, J. Bio. Mech. **9** (2008) 105–109.
5) O.Eytan and D.Elad, Analysis of intra-uterine fluid motion induced by uterine contractions, Bull. Math. Biol. **61** (1999) 221–238.
6) S.Srinivas and M.Kothandapani, Peristaltic transport in an asymmetric channel with heat transfer - A note, Int. Comm. Heat Mass Transfer. **35** (2008) 514–522.
7) R.Muthuraj and S.Srinivas, A note on heat transfer to MHD oscillatory flow in an asymmetric wavy channel, Int. Comm. Heat Mass Transfer. **37** (2010) 1255–1260.
8) V.K.Stokes, Couple stress in fluid. The Phy. Fl. **9** (1966) 1709-1715.
9) P.Chaturani, Viscosity of poiseulle flow of fluid with couple-stress with applications to blood flow, Biorheology **15** (1978) 119-128.
10) L.M.Srivastava, Peristaltic transport of a couple stress fluid, Biorheology **29** (1986) 153-166.
11) Kh.Mekheimer, Peristaltic transport of a couple stress fluid in a uniform and non- uniform channel, Biorheology **39** (2002) 755–765.
12) A.M.Sobh, Interaction of couple stresses and slip flow on peristaltic transport in uniform and non-uniform channels, Turkish J. Eng. Env. Sci. **32** (2008) 117 – 123.
13) S.U.S.Choi, Enhancing thermal conductivity of fluids with nanoparticles, ASME FED. **231** (1995) 99–105.
14) S.U.S.Choi, Z.G.Zhang, W.Yu, F.E.Lockwood and E.A.Grulke, Anomalously thermal conductivity enhancement in nanotube suspension, Appl. Phys. Lett. **79** (2001) 2252–2254.
15) J.Buongiorno, Convective transport in nanofluids, ASME J. Heat Trans. **128** (2006) 240–250.
16) S.Nadeem and S.Akram, Heat transfer in a peristaltic flow of MHD fluid with partial slip, Comm. Nonlin. Sci. Numer. Simulat. **15** (2010) 312–321.

17) Prakash, J., Siva, E.P., Tripathi, D., Kuharat, S. and Bég, O.A., 2019. Peristaltic pumping of magnetic nanofluids with thermal radiation and temperature-dependent viscosity effects: modelling a solar magneto-biomimetic nanopump. Renewable Energy, **133**, pp.1308-1326.

18) F.K.Landeghem, *K.*M.Hauff, *A.*Jordan, *K.T.*Hoffmann, *U.Gneveckow*, *R.Scholz*, *B.Thiesen*, *W.Bruck* and *A.*Deimling, Post-mortem studies in glioblastoma patients treated with thermotherapy using magnetic nanoparticles, J. Biomater. **30** (2009) 52–57.

19) D.Tripathi and O.A.Beg, A study on peristaltic flow of nanofluids: Application in drug delivery systems, Int. J. Heat Mass Transfer. **70** (2014) 61–70.

20) N.S.Akbar and S.Nadeem, Intestinal flow of a couple stress nanofluid in arteries, IEEE Trans. on Nano Biosci. **12** (2013) 332–339.

21) N.S.Akbar, S.Nadeem, T.Hayat and A.A.Hendi, Peristaltic flow of a nanofluid with slip effects, Meccanica **47** (2012) 1283–1294.

22) N.S.Akbar, S.Nadeem, T.Hayat and A.A.Hendi, Peristaltic flow of a nanofluid in a non-uniform tube, Heat Mass Transf. **48** (2012) 451–459.

23) N.S. Akbar, S. Nadeem and Z.H. Khan, Thermal and velocity slip effects on the MHD peristaltic flow with carbon nanotubes in an asymmetric channel: application of radiation therapy, Appl. Nano. Sci. **4** (2014) 849–857.

24) S. Nadeem and S. Ijaz, Influence of metallic nanoparticles on blood flow through arteries having both stenosis and aneurysm, Nano Biosci. **14** (2015) 668 - 679.

25) E.H.Aly and A.Ebaid, Effect of the velocity second slip boundary condition on the peristaltic flow of nanofluids in an asymmetric channel: Exact solution, Abst. And App. Anal. **2014** (2014) Article ID 191876, 11 pages doi:10.1155/2014/191876.

26) M.R.Habibi, M.Ghassemi and M.H.Hamedi, Analysis of high gradient magnetic field effects on distribution of nanoparticles injected into pulsatile blood stream, J. Magn. Magn. Mater. **324** (2012) 1473–1482.

27) Deepalakshmi, P., Siva, E.P., Tripathi, D., Bég, O.A. and Kuharat, S., 2024. MHD peristaltic two-phase Williamson fluid flow, heat and mass transfer through a ureteral tube with microliths: Electromagnetic therapy simulation. Numerical Heat Transfer, Part A: Applications, **85**(20), pp.1-24.

28) Deepalakshmi, P., Darvesh, A., Garalleh, H.A., Sánchez-Chero, M., Shankar, G. and Siva, E.P., 2024. Integrate mathematical modeling for heat dynamics in two-phase casson fluid

flow through renal tubes with variable wall properties. Ain Shams Engineering Journal, Article ID.103183, (In press).

29) Shankar, G., Siva, E.P., Tripathi, D. and Beg, O.A., Thermal analysis in unsteady oscillatory darcy blood flow through stenosed artery, International Journal of Thermofluids, **24**, p.100864, 2024.

30) Kothandapani, M., Prakash, J. and Srinivas, S., 2015. Peristaltic transport of a MHD Carreau fluid in a tapered asymmetric channel with permeable walls. International Journal of Biomathematics, **8**(04), p.1550054.

31) Shankar, G. and Siva, E.P., 2024. A Numerical Investigation of Thermal and Mass Exchange of Blood Along Porous Stenosis Arterial Flow With Applied Magnetic Field, IAENG International Journal of Applied Mathematics, **54**(3), 532-541.

32) Shankar G, Deepalakshmi P, Siva E.P, Tripathi D, Bég O.A, Thermomagnetic peristaltic Casson flow in a microchannel containing a Darcy–Brinkman porous medium under the influence of oscillatory, thermal radiation, slip and heat source effects. Pramana - Journal of Physics **99**, 32, 2025.

33) M. Kothandapani and J. Prakash, Effects of thermal radiation parameter and magnetic field on the peristaltic motion of Williamson nanofluids in a tapered asymmetric channel, Int. J. Heat Mass Transfer. **81** (2015) 234–245.

34) Rafiq, M.Y., Abbas, Z. and Ullah, M.Z., 2022. Peristaltic mechanism of couple stress nanomaterial in a tapered channel. Ain Shams Engineering Journal, 13(6), p.101779.

35) Khan, S.U., Shehzad, S.A., Rauf, A. and Ali, N., 2018. Mixed convection flow of couple stress nanofluid over oscillatory stretching sheet with heat absorption/generation effects. Results in Physics, 8, pp.1223-1231.

36) Alhazmi, S.E., Imran, A., Awais, M., Abbas, M., Alhejaili, W., Hamam, H., Alhowaity, A. and Waheed, A., 2022. Thermal convection in nanofluids for peristaltic flow in a nonuniform channel. Scientific Reports, 12(1), p.12656.

37) Nisar, Z., Hayat, T., Alsaedi, A. and Ahmad, B., 2023. Mathematical modeling for peristalsis of couple stress nanofluid. Mathematical Methods in the Applied Sciences, 46(10), pp.11683-11701.

38) Yasmin, H., Akram, S., Athar, M., Saeed, K., Razia, A. and Al-Juaid, J.G., 2024. Impact of multiple slips on thermally radiative peristaltic transport of Sisko nanofluid with double

diffusion convection, viscous dissipation, and induced magnetic field. Nanotechnology Reviews, 13(1), p.20240004.

39) Bilal, S., Akram, S., Athar, M., Saeed, K., Razia, A. and Riaz, A., 2024. Numerical analysis on theoretical model of magneto-Williamson nanofluid in relation to viscous dissipation, double-diffusion convection, thermal radiation and multiple slip boundaries. Pramana, 98(3), p.125.
40) Bilal, S., Akram, S., Athar, M., Saeed, K., Riaz, A. and Razia, A., 2024. Dissipative and multiple slips on thermally radiative biological fluid of magneto-six-constant Jeffrey nanofluid with double diffusion convection: a numerical investigation. BioNanoScience, 14(3), pp.2248-2263.
41) Akram, S., Saeed, K., Athar, M., Riaz, A., Razia, A. and Al-Malki, M.A., 2025. Enhancing retention of biological fluid transport of magnetized thermal radiative pseudoplastic nanofluid with double diffusion convection, viscous dissipation and boundary slips. Particulate Science and Technology, 43(1), pp.1-14.
42) Akram, S., Athar, M., Saeed, K., Riaz, A., Razia, A. and Alhamzi, G., 2024. Numerical simulation of double diffusion convection in a six-constant Jeffreys nanofluid with an inclined magnetic field and viscous dissipation: Multiple slips and thermal radiation analysis with peristalsis. AIP Advances, 14(7).
43) Akram, S., Saeed, K., Athar, M., Riaz, A., Razia, A. and Al-Malki, M.A., 2025. Interaction of induced magnetic field, double diffusion convection and multiple slips for thermal radiative biological flow of six-constant Jeffreys nanofluid: Advancements in mechanics. Separation Science and Technology, 60(2), pp.316-339.
44) Akram, S., Athar, M., Saeed, K. and Umair, M.Y., 2024. Double-diffusive convection with peristaltic wave in Sisko fluids along with inclined magnetic field and channel. Waves in Random and Complex Media, 34(5), pp.3789-3811.
45) Deepalakshmi, P., Shankar, G., Siva, E.P., Tripathi, D., Beg, O.A., Santra, S.S., Nandi, S. and Alotaibi, H., 2025. Thermally driven Two-phase shear thinning Non-Newtonian fluid through the Renal tube induced by Electric double layer effects with variable wall properties. Chinese Journal of Physics.

Appendix.

$$c_1=\frac{\beta}{\xi f_2}\left(h_1+\gamma\right)-c_2\left(1-\gamma f_2\right)e^{-f_2h_1},c_2=\frac{1-\frac{\beta}{\xi f_2}\left(h_1-h_2+2\gamma\right)}{\left(1+\gamma f_2\right)e^{-f_2h_2}-\left(1-\gamma f_2\right)e^{-f_2h_1}}$$

$$c_3=\frac{1+\frac{N_tc_2}{N_b}\left[\left(1+\gamma_1f_2\right)e^{-f_2h_2}-\left(1-\gamma_1f_2\right)e^{-f_2h_1}\right]}{h_2-h_1-2\gamma_1},c_4=\frac{N_tc_2}{N_b}\left(1-\gamma_1f_2\right)e^{-f_2h_2}-c_3\left(h_1+\gamma_1\right)$$

$$f_4=\frac{BrN_tc_2f_2}{N_b}-c_2Grf_2,\ f_5=c_3Br-\frac{Gr\beta}{\xi f_2},\ f_6=f_2^6-S^2\left(f_2^4\right)+H^2S^2\left(f_2^2\right),\ f_7=\frac{S^2f_4}{f_6},\ f_8=\frac{f_5}{2H^2}$$

$$l_1=A\sinh Ah_1+LA^2\cosh Ah_1,l_2=A\cosh Ah_1+LA^2\sinh Ah_1$$

$$l_3=B\sinh Bh_1+LB^2\cosh Bh_1,l_4=B\cosh Bh_1+LB^2\sinh Bh_1$$

$$l_5=2f_8h_1+2Lf_8-\left(f_7f_2-Lf_7f_2^2\right)e^{-f_2h_1}$$

$$l_6=A\sinh Ah_2-LA^2\cosh Ah_2,l_7=A\cosh Ah_2-LA^2\sinh Ah_2$$

$$l_8=B\sinh Bh_2-LB^2\cosh Bh_2,l_9=B\cosh Bh_2-LB^2\sinh Bh_2$$

$$l_{10}=2f_8h_2-2Lf_8-\left(f_7f_2+Lf_7f_2^2\right)e^{-f_2h_2}$$

$$D_1=h_1-h_2,D_2=\cosh Ah_1-\cosh Ah_2,D_3=\sinh Ah_1-\sinh Ah_2$$

$$D_4=\cosh Bh_1-\cosh Bh_2,D_5=\sinh Bh_1-\sinh Bh_2$$

$$B_1=F-f_8\left(h_1^2-h_2^2\right)-f_7\left(e^{-f_2h_1}-e^{-f_2h_2}\right),B_2=-l_5,B_3=-l_{10}$$

$$l_{11}=A^3\sinh Ah_1,l_{12}=A^3\cosh Ah_1,l_{13}=B^3\sinh Bh_1,l_{14}=B^3\cosh Bh_1$$

$$l_{15}=A^3\sinh Ah_2,l_{16}=A^3\cosh Ah_2,l_{17}=B^3\sinh Bh_2,l_{18}=B^3\cosh Bh_2,B_4=f_7f_2^3e^{-f_2h_1},B_5=f_7f_2^3e^{-f_2h_2}$$

$$l_{19}=D_1l_1-D_2,l_{20}=D_1l_2-D_3,l_{21}=D_1l_3-D_4,l_{22}=D_1l_4-D_5,B_6=D_1B_2-B_1$$

$$l_{23}=D_1l_6-D_2,l_{24}=D_1l_7-D_3,l_{25}=D_1l_8-D_4,l_{26}=D_1l_9-D_5,B_7=D_1B_3-B_1$$

$$l_{27}=l_{24}-\frac{l_{23}}{l_{19}}l_{20},l_{28}=l_{25}-\frac{l_{23}}{l_{19}}l_{21},l_{29}=l_{26}-\frac{l_{23}}{l_{19}}l_{22},l_{30}=l_{12}-\frac{l_{11}}{l_{19}}l_{20},l_{31}=l_{13}-\frac{l_{11}}{l_{19}}l_{21}$$

$$l_{32}=l_{14}-\frac{l_{11}}{l_{19}}l_{22},l_{33}=l_{16}-\frac{l_{15}}{l_{19}}l_{20},l_{34}=l_{17}-\frac{l_{15}}{l_{19}}l_{21},l_{35}=l_{18}-\frac{l_{15}}{l_{19}}l_{22},B_8=B_7-\frac{l_{23}}{l_{19}}B_6$$

$$B_9=B_4-\frac{l_{11}}{l_{19}}B_6,B_{10}=B_5-\frac{l_{15}}{l_{19}}B_6,l_{36}=l_{31}-\frac{l_{30}}{l_{27}}l_{28},l_{37}=l_{32}-\frac{l_{30}}{l_{27}}l_{29},B_{11}=B_9-\frac{l_{30}}{l_{27}}B_8$$

$$l_{38}=l_{34}-\frac{l_{33}}{l_{27}}l_{28},l_{39}=l_{35}-\frac{l_{33}}{l_{27}}l_{29},B_{12}=B_{10}-\frac{l_{33}}{l_{27}}B_8$$

$$c_{10}=\frac{l_{36}B_{12}-l_{38}B_{11}}{l_{36}l_{39}-l_{38}l_{37}},c_9=\frac{B_{11}-l_{37}c_{10}}{l_{36}},c_8=\frac{B_8-l_{28}c_9-l_{29}c_{10}}{l_{27}},c_7=\frac{B_6-l_{20}c_8-l_{21}c_9-l_{22}c_{10}}{l_{19}}$$

$$c_6 = \frac{B_1 - D_2 c_7 - D_3 c_8 - D_4 c_9 - D_5 c_{10}}{D_1}$$

$$f_9 = c_7\left(A^3 - \frac{A^5}{S^2} - H^2 A\right),\ f_{10} = c_8\left(A^3 - \frac{A^5}{S^2} - H^2 A\right),\ f_{11} = c_9\left(B^3 - \frac{B^5}{S^2} - H^2 B\right),$$

$$f_{12} = c_{10}\left(B^3 - \frac{B^5}{S^2} - H^2 B\right),\ f_{13} = \frac{f_7 f_2^5}{S^2} - f_7 f_2^3 + H^2 f_7 f_2 + c_2 Gr - \frac{BrN_t}{N_b} c_2$$

$$f_{14} = c_3 Br - 2H^2 f_8 - \frac{Gr\beta}{\xi f_2},\ f_{15} = c_1 Gr + c_4 Br - c_6 H^2$$

Credit Author Statement:

P. Deepalakshmi: *Writing – original draft, Conceptualization,* ***G. Shankar:*** *Writing – review & editing, Methodology,* ***E.P. Siva:*** *Visualization, Supervision, Investigation,* ***D. Tripathi:*** *Validation, Formal analysis,* ***O. Anwar Beg:*** *Data curation. Writing – review & editing*

Conflict of Interest Statement:

The authors reported no conflicts of interest.